Analytical investigation of railway overhead contact wire dynamics and comparison with experimental results

Analytical investigation of railway overhead contact wire dynamics and comparison with experimental results

D. Anastasio, A. Fasana, L. Garibaldi, S. Marchesiello*

* *Department of Mechanical and Aerospace Engineering, Politecnico di Torino, Corso Duca degli Abruzzi 24, 10129 Torino, Italy.*

https://doi.org/10.1016/j.ymssp.2018.06.021

Cite as:

D. Anastasio, A. Fasana, L. Garibaldi, S. Marchesiello, Analytical investigation of railway overhead contact wire dynamics and comparison with experimental results, Mechanical Systems and Signal Processing 116 (2019) 277-292.

Corresponding author. Tel.: +390110906947: fax: +390110906999; e-mail address: stefano.marchesiello@polito.it

ABSTRACT

In this paper an analytical method for studying the free response of continuous vibrating systems with distributed and possibly non-proportional viscous damping is proposed. The most general case the method refers to is a piece-wise homogeneous Euler-Bernoulli beam, with lumped elastic and inertial elements and subjected to tensile load. The practical application of the method to a contact wire is also presented, aiming at analysing its dynamic response. Contact wires are typically used in the overhead contact line of the railway electrification system but, despite their wide diffusion, their damping properties have not been exhaustively studied. This study aims at experimentally validate the analytical method to define a reliable dynamic model of overhead contact lines.

The wire is modelled as an axially loaded homogeneous beam, with lumped elastic and inertial elements (i.e. droppers and clamps). A state-form expansion applied in conjunction with a transfer matrix technique is adopted to extract the eigenvalues and to express the eigenfunctions in analytical form. Experimental measurements have been carried out in the Dynamics & Identification Research Group (DIRG) laboratory of Politecnico di Torino considering two different damping scenarios, and the modal properties of the test bench have been extracted by using a linear subspace identification technique. The damping distribution is finally investigated starting from the experimental data, in order to seek for the most appropriate damping model.

KEYWORDS: overhead contact line; damping distribution; non-proportional damping; stochastic subspace identification; analytical investigation.

1. INTRODUCTION

Contact wires are widely used in the overhead contact lines of railway electrification systems, and typically consist of long and flexible copper cables, with a particular cross section to allow the connection with the droppers. An extensive literature has been produced about the characterization of contact wires and overhead contact lines. Indeed, tests on the field are quite difficult to be performed and a proper model is fundamental in order to correctly simulate the dynamic evolution of the system. In [1] general indications about the modeling of an overhead contact line are presented, and a comparison between a string model and a Euler-Bernoulli beam model is carried out. The latter proved to be more effective, even because its dispersive wave characteristics better represents the behavior of the contact wire [2]. In [3] an analytical study on the effects of a moving force, representing the pantograph, has been conducted adopting a beam model. In spite of the high number of studies on the dynamics of contact wires, their damping properties have been not exhaustively investigated. Overhead contact lines are usually considered

low-damped systems, and in many cases damping is suggested to be negligible at all [4]. This is a gross approximation that can lead to unreliable results, especially when adopting a finite element model [5]. In particular, the influence of damping has been studied in [6, 7], showing its considerable effects on the quality of the current collection for high speed trains. Recently, a benchmark has been proposed [8] to model the pantograph-catenary interaction. Proportional structural damping is considered in this study with coefficients $\alpha = 0.0125\ s^{-1}$, $\beta = 10^{-4}\ s$ obtained from measurements on the Italian high-speed catenary. In [9] the identification of damping of Norwegian overhead contact lines has been performed under different operational conditions. In [10] experimental measurements of the damping ratios have been conducted, leading to define a range from 0.01 to 0.04.

In this paper, a twofold purpose is chased: presenting an analytical method for better investigating the damping distribution and using experimental measurements to validate the predictions of the model.

The presented method can generally handle several kinds of continuous vibrating systems with either proportional and non-proportional damping. It is based on [11, 12], and uses a partition of the continuous system in homogeneous substructures (or segments) in conjunction with a transfer matrix technique. In the particular case of overhead contact lines, each section corresponds to the distance between two consecutive droppers, the latter being modeled as lumped elastic elements. A key feature of overhead contact lines is the tensile force acting on both contact wire and messenger wire, thus the reference method is here extended to account for an axial load across the segments of the considered structure. The proposed approach leads to an easy implementation and presents a high computational efficiency, due to the invariance of the matrix dimensions with respect to the number of segments considered. Experimental measurements have also been performed at the DIRG laboratory of the Politecnico di Torino considering two different damping scenarios. A linear subspace identification technique [13 - 15] is used to extract the modal parameters from the acquired data, and a model updating process is implemented to find the best-fit between experimental results and analytical predictions. The damping distribution is finally analyzed combining information from both the experimental outcomes and the presented analytic model.

2. MODAL ANALYSIS OF CONTINUOUS SYSTEMS WITH VISCOUS GENERALIZED DAMPING AND TENSILE FORCE

The dynamic behavior of a continuous system with viscous generalized damping can be described, recalling [11], by the following equation of motion:

$$M\left[\frac{\partial^2}{\partial t^2}w(\mathbf{x},t)\right]+C\left[\frac{\partial}{\partial t}w(\mathbf{x},t)\right]+K[w(\mathbf{x},t)]=f(\mathbf{x},t),\quad \mathbf{x}\in\mathcal{D} \tag{1}$$

Where *M*, *C*, *K*, are linear homogeneous differential operators and are referred to as mass, damping and stiffness operator respectively, *f* is the external force density, *w* and **x** are the displacement and the spatial coordinate in a domain of extension $\mathcal{D}$, and *t* is time.

The differential eigenvalue problem associated with eq. 1 has been already solved in [11] considering a piece-wise constant Euler-Bernoulli beam with both internal and external damping distribution. In this case, the mass and the stiffness operator are:

$$M=m(x),\quad K=\frac{\partial^2}{\partial x^2}\left[k(x)\frac{\partial^2}{\partial x^2}\right] \tag{2}$$

Where $m(x)$ is the mass per unit length of the beam and $k(x)=EI(x)$ is the bending stiffness, *E* being the Young's Modulus and *I* the area moment of inertia.

The damping operator can be a general external distributed viscous damping function $C=c_{ex}(x)$ or can be expressed according to the Kelvin-Voigt model [16] as:

$$C=\frac{\partial^2}{\partial x^2}\left[c_{in}(x)\frac{\partial^2}{\partial x^2}\right] \tag{3}$$

In particular, damping is said to be proportional when the damping operator can be expressed as a linear combination of the mass operator and the stiffness operator.

According to the equations above, considering both an external and an internal damping distribution, the equation of a Euler-Bernoulli beam in bending vibration under a distributed transverse force is obtained.

$$m(x)\frac{\partial^2 w}{\partial t^2}+c_{ex}(x)\frac{\partial w}{\partial t}+\frac{\partial^2}{\partial x^2}\left[c_{in}(x)\frac{\partial^2}{\partial x^2}\left(\frac{\partial w}{\partial t}\right)\right]+\frac{\partial^2}{\partial x^2}\left[k(x)\frac{\partial^2 w}{\partial x^2}\right]=f \tag{4}$$

Where $f=f(x,t)$ is the transverse force and $w=w(x,t)$ is the transverse displacement. If a tensile load is applied to the beam, the equation is modified in this paper to include the axial force T (positive in tension), as follows:

$$m(x)\frac{\partial^2 w}{\partial t^2}+c_{ex}(x)\frac{\partial w}{\partial t}+\frac{\partial^2}{\partial x^2}\left[c_{in}^{k}(x)\frac{\partial^2}{\partial x^2}\left(\frac{\partial w}{\partial t}\right)\right]-c_{in}^{T}\frac{\partial^2}{\partial x^2}\left(\frac{\partial w}{\partial t}\right)+\frac{\partial^2}{\partial x^2}\left[k(x)\frac{\partial^2 w}{\partial x^2}\right]-\mathrm{T}\frac{\partial^2 w}{\partial x^2}=f(x,t) \tag{5}$$

The internal damping distribution is now described by two coefficients, c_{in}^{k} and c_{in}^{T}, as an extension of the Kelvin-Voigt model (eq. 3) to the axially loaded case. Two boundary conditions must be satisfied at x=0 and x=L, with L being the length of the beam.

2.1. **The differential eigenvalue problem**

If no external force is present, eq. 5 reduces to:

$$m(x)\frac{\partial^2 w}{\partial t^2} + c_{ex}(x)\frac{\partial w}{\partial t} + \frac{\partial^2}{\partial x^2}\left[c_{in}^{k}(x)\frac{\partial^2}{\partial x^2}\left(\frac{\partial w}{\partial t}\right)\right] - c_{in}^{T}\frac{\partial^2}{\partial x^2}\left(\frac{\partial w}{\partial t}\right) + \frac{\partial^2}{\partial x^2}\left[k(x)\frac{\partial^2 w}{\partial x^2}\right] - \mathrm{T}\frac{\partial^2 w}{\partial x^2} = 0 \tag{6}$$

The solution is sought by separating the variables in the form:

$$w(x,t) = \phi(x)q(t), \quad q(t) = q_0 e^{st} \tag{7}$$

Where the constant s has to be determined so that the boundary conditions are satisfied.

The beam is divided in N segments of length $\Delta x_p = x_p - x_{p-1}$ (where x_0=0 and x_N=L) in which $m(x), c_{ex}(x), c_{in}^{k}(x)$ and $k(x)$ are assumed to be constant. The coefficient c_{in}^{T} is constant along the all beam, as T is constant. Eq. 6 is separated in N equations that can be written in the form:

$$\phi_p^{\mathrm{IV}} = -\frac{m_p s^2 + c_{ex,p}s}{k_p + c_{in,p}^{k}s}\phi_p + \frac{T + c_{in}^{T}s}{k_p + c_{in,p}^{k}s}\phi_p^{\mathrm{II}} = -\sigma_p\phi_p + \gamma_p\phi_p^{\mathrm{II}} \tag{8}$$

The problem is solved adopting the state-form, and a state vector $\mathbf{y}(x)$ is defined as follows:

$$\mathbf{y}(x) = [\phi^{III}(x) \quad \phi^{II}(x) \quad \phi^{I}(x) \quad \phi(x)]^{\mathrm{T}} \tag{9}$$

Eq. 8 then becomes:

$$\mathbf{y}_{\mathrm{p}}^{\mathrm{I}}(x) = \mathbf{S}_{\mathrm{p}}\mathbf{y}_{\mathrm{p}}(x) \tag{10}$$

Where $\mathbf{S}_{\mathrm{p}}$ is the companion matrix:

$$\mathbf{S}_{\mathrm{p}} = \begin{bmatrix} 0 & \gamma_p & 0 & -\sigma_p \\ 1 & 0 & 0 & 0 \\ 0 & 1 & 0 & 0 \\ 0 & 0 & 1 & 0 \end{bmatrix} \tag{11}$$

The four eigenvalues of the companion matrix are:

$$\lambda_{p_{1,2}} = \pm\sqrt{\frac{\gamma_p + \sqrt{\gamma_p^2 - 4\sigma_p}}{2}}, \qquad \lambda_{p_{3,4}} = \pm\sqrt{\frac{\gamma_p - \sqrt{\gamma_p^2 - 4\sigma_p}}{2}} \tag{12}$$

While the pth segment eigenvectors matrix $\mathbf{\Phi}_p$ is:

$$\boldsymbol{\Phi}_p = \begin{bmatrix} \lambda_{p_1}^3 & \lambda_{p_2}^3 & \lambda_{p_3}^3 & \lambda_{p_4}^3 \\ \lambda_{p_1}^2 & \lambda_{p_2}^2 & \lambda_{p_3}^2 & \lambda_{p_4}^2 \\ \lambda_{p_1} & \lambda_{p_2} & \lambda_{p_3} & \lambda_{p_4} \\ 1 & 1 & 1 & 1 \end{bmatrix} \tag{13}$$

Finally, the solution to eq. 10 can be written in the form:

$$\mathbf{y}_{\mathrm{p}}(x) = \boldsymbol{\Phi}_p e^{\boldsymbol{\Lambda}_p x} \mathbf{c}_{\mathrm{p}} \tag{14}$$

Where $\boldsymbol{\Lambda}_p$ is the eigenvalues matrix of the *p*th segment and $\mathbf{c}_{\mathrm{p}}$ is the constants vector. The solution $\mathbf{y}_{\mathrm{p}}(x)$ is valid when $x \in [x_{p-1}, x_p]$, thus the constants vector of the *p*th segment can be calculated knowing $\mathbf{y}_{\mathrm{p}}(x_{p-1})$.

2.2. **The boundary conditions**

According to Ref. [11], the boundary conditions at the ends of the beam can be written in the form:

$$\begin{aligned} &\mathbf{B}_{\mathrm{e0}} \mathbf{y}_1(0) = \mathbf{0} \\ &\mathbf{B}_{\mathrm{eL}} \mathbf{y}_{\mathrm{N}}(L) = \mathbf{0} \end{aligned} \tag{15}$$

Where $\mathbf{B}_{\mathrm{e0}}$ and $\mathbf{B}_{\mathrm{eL}}$ are two matrices depending on the kind of constraints. For a clamped end, a pinned end, and a free end, those matrices are simply:

$$\mathbf{B}_{\mathrm{e}} = \begin{bmatrix} 0 & 0 & 1 & 0 \\ 0 & 0 & 0 & 1 \end{bmatrix}, \quad \mathbf{B}_{\mathrm{e}} = \begin{bmatrix} 0 & 1 & 0 & 0 \\ 0 & 0 & 0 & 1 \end{bmatrix}, \quad \mathbf{B}_{\mathrm{e}} = \begin{bmatrix} 1 & 0 & 0 & 0 \\ 0 & 1 & 0 & 0 \end{bmatrix} \tag{16}$$

Clamped Pinned Free

Moreover, boundary constraints must be imposed at the interface between two consecutive segments as follows:

$$\mathbf{y}_{\mathrm{p}}(x_{p-1}) = \mathbf{B}_{\mathrm{p}-1} \mathbf{y}_{\mathrm{p}-1}(x_{p-1}), \quad p = 2, \dots, N \tag{17}$$

Where $\mathbf{B}_{\mathrm{p}-1}$ is a matrix obtained imposing the continuity of displacements, rotation, moment and shear at each interface and can be written in the following form:

$$\mathbf{B}_{\mathrm{p}-1} = \begin{bmatrix} b_p^{-1} b_{p-1} & 0 & 0 & -b_p^{-1} r_{p-1}^w \\ 0 & b_p^{-1} b_{p-1} & -b_p^{-1} r_{p-1}^\theta & 0 \\ 0 & 0 & 1 & 0 \\ 0 & 0 & 0 & 1 \end{bmatrix} \tag{18}$$

Where b_p and b_{p-1} depend on internal stiffness and damping, i.e.:

$$b_p = c_{in,p}^k s + k_p \tag{19}$$

While r^w and r^θ depend on external constraints. If in x_{p-1} there are external constraints, such as lumped inertia, damping or stiffness elements, then:

$$r^w = M_w s^2 + C_w s + K_w$$
$$r^\theta = K_\theta \tag{20}$$

Where M_w, C_w, K_w represent a lumped mass, a lumped damper and a lumped stiffness respectively, while K_θ is a lumped rotational stiffness. It is worth noticing that these elements can represent the droppers (with their clamps) of the overhead contact line.

Taking into account the boundary conditions, eq. 14 can be written as:

$$\mathbf{y}_{\mathrm{p}}(x) = \boldsymbol{\Phi}_p e^{\boldsymbol{\Lambda}_p(x_p - x_{p-1})} \boldsymbol{\Phi}_p^{-1} \mathbf{B}_{\mathrm{p}-1} \mathbf{y}_{\mathrm{p}-1}(x_{p-1}) \tag{21}$$

With $\mathbf{B}_0 = \mathbf{I}$ and $\boldsymbol{\Phi}_p^{-1}$ can be obtained by:

$$\boldsymbol{\Phi}_p^{-1} = \frac{1}{2\lambda_{p_1}\lambda_{p_2}(\lambda_{p_1}^2 - \lambda_{p_2}^2)} \begin{bmatrix} \lambda_{p_2} & \lambda_{p_1}\lambda_{p_2} & -\lambda_{p_2}^3 & -\lambda_{p_1}\lambda_{p_2}^3 \\ -\lambda_{p_1} & -\lambda_{p_1}\lambda_{p_2} & \lambda_{p_1}^3 & \lambda_{p_1}^3\lambda_{p_2} \\ \lambda_{p_2} & \lambda_{p_1}\lambda_{p_2} & \lambda_{p_2}^3 & -\lambda_{p_1}\lambda_{p_2}^3 \\ \lambda_{p_1} & -\lambda_{p_1}\lambda_{p_2} & -\lambda_{p_1}^3 & \lambda_{p_1}^3\lambda_{p_2} \end{bmatrix} \tag{22}$$

Moreover, eq. 21 yields:

$$\mathbf{y}_{\mathrm{p}}(x) = \prod_{i=p}^{1} [\boldsymbol{\Phi}_i e^{\boldsymbol{\Lambda}_i(x_i - x_{i-1})} \boldsymbol{\Phi}_i^{-1} \mathbf{B}_{\mathrm{i}-1}] \mathbf{y}_1(0) = \boldsymbol{\Pi}_p(x_p) \mathbf{y}_1(0), \quad p = 1, \dots, N \tag{23}$$

The matrix $\boldsymbol{\Pi}_p$ is a transfer matrix, which allows eq. 15 to be written as:

$$\begin{cases} \mathbf{B}_{\mathrm{e0}} \boldsymbol{\Phi}_1 \mathbf{c}_1 = 0 \\ \mathbf{B}_{\mathrm{eL}} \boldsymbol{\Pi}_{\mathrm{N}}(L) \boldsymbol{\Phi}_1 \mathbf{c}_1 = 0 \end{cases} \quad \text{or} \quad \boldsymbol{\Theta} \mathbf{c}_1 = \mathbf{0} \tag{24}$$

Eq. 24 has non-trivial solutions only if the determinant of the coefficient matrix is zero:

$$\det(\boldsymbol{\Theta}(s_n)) = 0, \quad n = 1, 2, \dots \tag{25}$$

Where n is the mode number. The solutions to the last equation are also the solutions to the eigenvalue problem related to eq. 6, and if the system is underdamped they form an infinite set of complex conjugate pairs s_n, s_n^* of discrete values, with $s_n = -\zeta_n \omega_n + i\omega_n\sqrt{1 - \zeta_n^2}$. The following relations provide the modal frequencies and the modal damping factors respectively:

$$\omega_n = |s_n|, \quad \zeta_n = -\frac{\Re[s_n]}{|s_n|} \tag{26}$$

Recalling that $\boldsymbol{\Theta}$ is a 4x4 complex matrix, the solutions to the eigenvalue problem $\det(\boldsymbol{\Theta}) = 0$ can be found using an appropriate root-finding algorithm that works in the complex domain. Alternatively, the complex function can be split into its real and imaginary parts, so that the root-finding problem reduces to:

$$\boldsymbol{\Psi}\big(\boldsymbol{\Theta}(s_n)\big)\boldsymbol{\varsigma}(s_n) = \mathbf{0} \tag{27}$$

Where:

$$\boldsymbol{\Psi} = \big[\Re[\det(\boldsymbol{\Theta})] \quad \Im[\det(\boldsymbol{\Theta})]\big], \quad \boldsymbol{\varsigma} = \big[\Re[s_n] \quad \Im[s_n]\big]^{\mathrm{T}} \tag{28}$$

It is worth noticing that s_n is imaginary in the undamped case, leading to an easy root-finding problem in one variable. The undamped solutions therefore can be taken as a starting point in eq. 27, for instance applying the Newton method [17]. If $\boldsymbol{\varsigma}_0$ is the starting point and **J** is the Jacobian matrix (2x2) of the function $\boldsymbol{\Psi}$, the iterative process can be written as:

$$\boldsymbol{\varsigma}_k = \boldsymbol{\varsigma}_{k-1} - \mathbf{J}_{\mathrm{k-1}}^{-1}\boldsymbol{\Psi}_{\mathrm{k-1}}, \quad k = 1,2,\ldots \tag{29}$$

The iterations proceed until $|\boldsymbol{\varsigma}_{k^*} - \boldsymbol{\varsigma}_{k^*-1}| < \varepsilon$, with ε desired tolerance, yielding $s_n = \varsigma_{k^*}(1) + i\varsigma_{k^*}(2)$.

3. THE EXPERIMENTAL SETUP

Experiments have been carried out using a 30 m long railway contact wire in order to both test the method and analyze the damping distribution of the system in several operational conditions. The experimental setup is shown in Fig. 1.

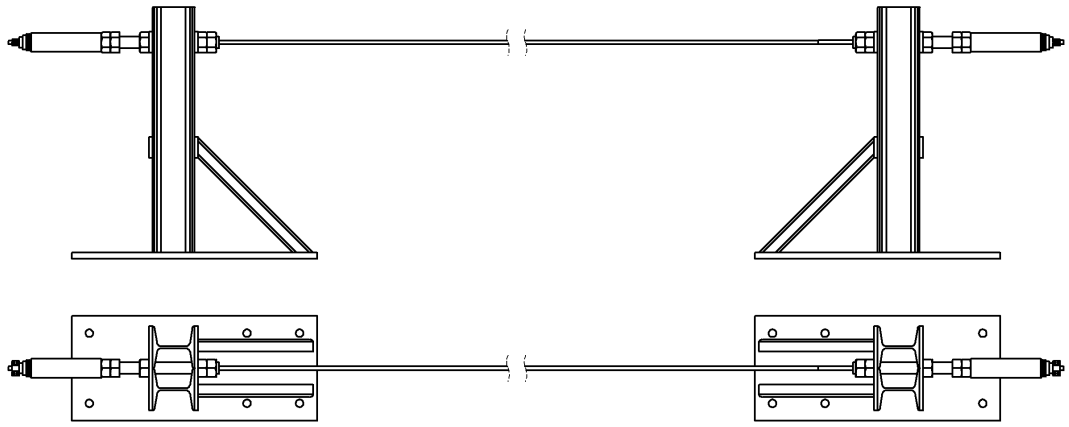

Fig. 1: The experimental setup.

The tensile force is applied to the wire by means of the tensioning device shown in Fig. 2, which is based on a simple screw-nut mechanism. A load cell is used to measure the applied tension and a thrust bearing on each end is used to assure that no torsion is transferred to the wire. The adopted system of reference is shown in Fig. 2 and the properties of the adopted contact wire are summarized in Table 1.

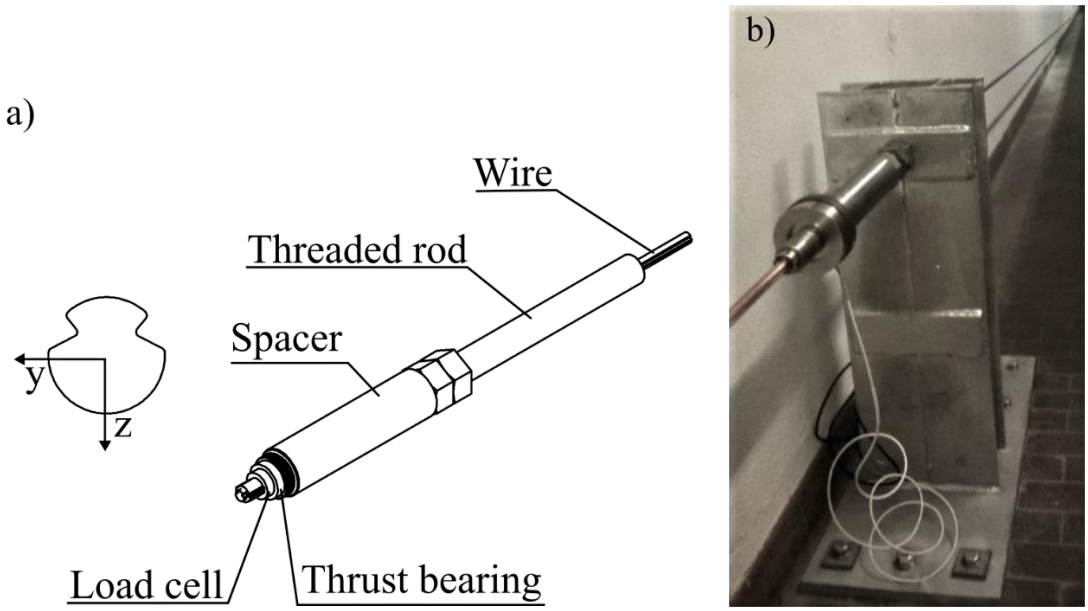

Fig. 2: a) Scheme of the tensioning device and section of the contact wire. b) Photo of the test bench.

Properties of the contact wire [18]	
Material	Cu-ETP
Section (mm^2)	100
Mass per unit length (kg/m)	0.889
Young's Modulus (GPa)	120
Distance between the supports (m)	30.7

Table 1: Properties of the contact wire

3.1. **Contact wire without lumped elements**

The first experimental setup consists of a simple contact wire under axial load, and it is aimed to characterize its damping properties. All the following tests are performed applying an impulse load along the z-axis and recording the accelerations of four different points on the wire along the three directions. The position of the accelerometers is reported in Table 2. The acquisition time is set to $300\ s$ for all the tests to ensure that a sufficient number of oscillations are recorded for the low-frequency modes. Furthermore, different levels of tension are considered according to Table 3.

Accelerometer n°	1	2	3	4
Position (m)	1.5	9	17	27

Table 2: Position of the accelerometers measured from the left end (case without lumped elements).

Test	Tensile load T (kN)	Sampling frequency f_s (Hz)	Acquisition time t (s)
1	$5.17 \pm 6\ 10^{-3}$	81.92	300
2	$10.95 \pm 3\ 10^{-2}$	81.92	300
3	$16.24 \pm 7\ 10^{-2}$	81.92	300

Table 3: Tests performed on the contact wire. The tensile load is written as mean value ± variation.

Because of the considerable length of the wire, vibrations occur on both the z-axis and the y-axis when applying an impulse load along the z-axis. Furthermore, the section of the wire is not axisymmetric; thus the bending natural frequencies along the two axes are slightly different. Fig. 3 shows the power spectral density of the acceleration recorded by the z-channel and the y-channel of the second accelerometer during Test 3. The zoomed area clearly shows two very close peaks, one mainly present on the z-axis and the other on the y-axis. These *twin modes* are very frequent in this kind of systems and must be correctly recognized in order to extract the modal parameters of interest, which in this case are related to the z-axis only (the flexural displacement is called w in eq. 1).

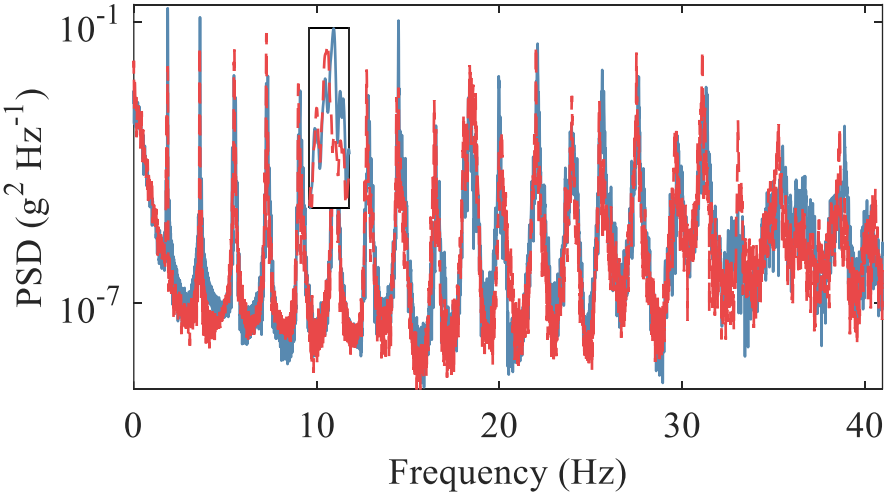

Fig. 3: Power spectral density of the acceleration recorded by the second accelerometer during the test 3. Solid blue line: z-axis. Dashed red line: y-axis.

3.1.1. System identification

A linear subspace identification technique [13] is used to extract the modal parameters from the described system, considering the output-only case. The accelerations recorded along the x-axis are discarded; thus a total of 8 channels (4 along the z-axis and 4 along the y-axis) are taken into account for each test. The identified poles are collected for each model order of the method, and stability is checked by setting thresholds for frequencies, damping ratios and mode shapes [15]. The stabilization diagram related to Test 1 is reported in Fig. 4. Because of the high number of modes present in the frequency range of interest 0-40 Hz, it is compulsory to select the model order carefully, and therefore the modal parameters, for each physical mode. Two different criteria for order selection are compared to obtain the best possible results:

C1. The model order for each mode is selected according to the value of the damping ratio that is the median value of the damping ratios related to that mode.

C2. The model order for each mode is selected comparing the MACs between the mode shapes related to that mode and considering the order that achieves the best MACs.

Furthermore, the main direction of each mode shape is evaluated, in order to discard the modes related to the y-axis. Table 4 summarizes the identified modes according to the two criteria for Test 1.

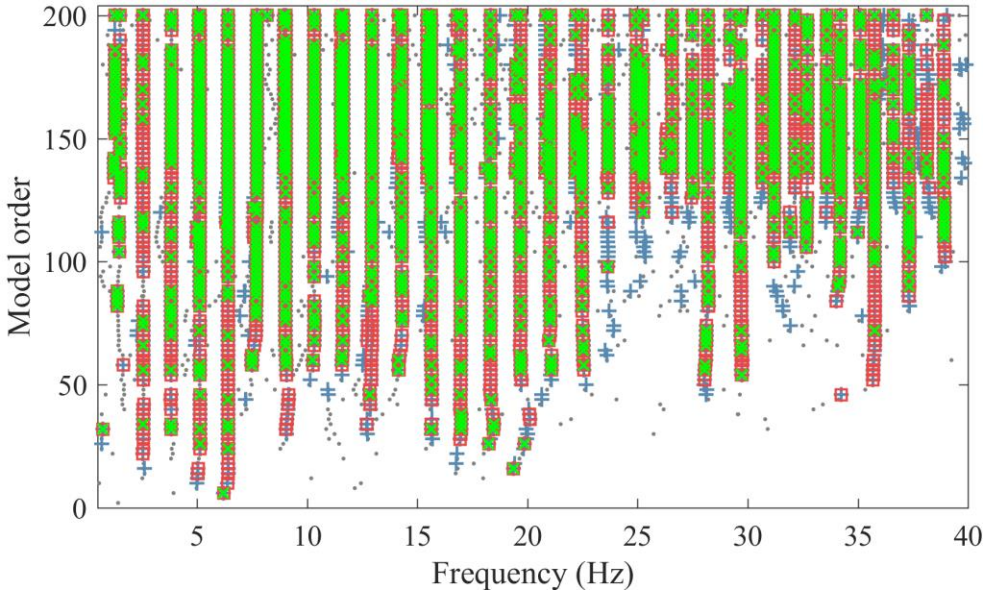

Fig. 4: Stabilization diagram for Test 1. Stabilization thresholds for natural frequency, damping ratio and MAC are 0.5%, 10% and 99.5%, respectively. Grey dot: new (not stable) pole. Blue plus: pole stable in frequency. Red square: pole stable in frequency and MAC (Modal Assurance Criterion). Green cross: pole stable in frequency, MAC and damping.

Frequency, f_{exp} (Hz)		Damping ratio, ζ_{exp} (%)	
C1	C2	C1	C2
1.528	1.524	0.697	0.561
2.565	2.565	0.012	0.013
3.854	3.854	0.033	0.033
5.097	*5.097*	*0.037*	*0.033*
5.137	5.137	0.019	0.020
6.424	6.424	0.024	0.025
7.717	7.714	0.055	0.068
8.944	*8.943*	*0.046*	*0.030*
9.020	9.020	0.050	0.050
10.318	10.313	0.057	0.079
11.532	*11.533*	*0.023*	*0.025*
11.633	11.633	0.038	0.041
12.941	12.942	0.022	0.016
14.288	14.286	0.030	0.052
15.462	*15.462*	*0.029*	*0.025*
15.623	15.623	0.029	0.031
16.976	16.977	0.021	0.026
18.326	18.330	0.022	0.028
19.487	*19.489*	*0.039*	*0.030*
19.683	19.690	0.027	0.028
20.835	*20.825*	*0.076*	*0.108*
21.040	21.039	0.049	0.038
22.195	*22.196*	*0.047*	*0.049*
22.474	22.474	0.023	0.019
23.680	23.678	0.040	0.042
24.947	*24.946*	*0.021*	*0.021*
25.242	25.243	0.145	0.141
26.570	26.587	0.093	0.073
27.507	*27.507*	*0.124*	*0.127*
28.216	28.218	0.028	0.026
29.207	*29.213*	*0.050*	*0.049*
29.681	29.681	0.037	0.038
30.659	*30.654*	*0.034*	*0.030*
31.185	31.184	0.052	0.054
32.139	*32.138*	*0.015*	*0.005*
32.702	32.700	0.021	0.020
33.589	*33.591*	*0.030*	*0.029*
34.205	34.203	0.052	0.049
35.104	*35.104*	*0.017*	*0.016*
35.756	35.755	0.025	0.019
36.600	*36.600*	*0.026*	*0.026*
37.315	37.323	0.026	0.061
38.897	38.899	0.026	0.022

Table 4: Identified modes for Test 1. Italics red color highlights modes related to the y-axis. C1 and C2 are the two different criteria.

The MACs between C1 and C2 are computed to verify that each identified mode shape is the same for the different criteria. The best order for each mode is then chosen according to C1.

The identified bending frequencies can be compared with the analytical bending frequencies of a simply-supported beam, obtained using eq. 30 [3] or computed with the presented method in the simple case of no lumped elements.

$$f_{a,j} = \frac{j}{2L}\sqrt{\frac{T}{m} + \left(\frac{j\pi}{L}\right)^2 \frac{EI}{m}}, \quad j = 1, 2, 3, \dots \tag{30}$$

A model updating process is therefore implemented in order to refine the parameters and obtain the best-fit results.

3.1.2. **Damping distribution and model updating**

An analysis of the damping distribution on the contact wire can be based on the identified poles to find a model that properly fits the experimental results. The simplest and most common damping distribution is the proportional damping, based on the hypothesis that damping can be expressed as a linear combination of the mass distribution and the stiffness distribution. With eq. 5, this hypothesis can be written as:

$$c_{ex}(x) = \alpha\, m(x), \quad c_{in}^{k}(x) = \beta\, k(x), \quad c_{in}^{T} = \beta\, T \quad \alpha, \beta \in \mathbb{R}^{+} \tag{31}$$

If such a model is adopted, experimental frequencies and damping ratios listed in Table 4 are the (undamped) natural frequencies and corresponding damping ratios, and their correlation is given by eq. 32, where $\omega_{exp} = 2\pi f_{exp}$. The two coefficients α and β can be obtained solving eq. 32 in a least-square sense, starting from experimental data.

$$\zeta_{exp,r} = \frac{\alpha}{2}\frac{1}{\omega_{exp,r}} + \frac{\beta}{2}\omega_{exp,r}, \quad r = 1,2, \dots, N \tag{32}$$

Fig. 5 compares the experimental damping ratios with the proportional damping model for each level of tension. A good match is obtained for the three tests, though some experimental values are not well caught by the assumed damping model. This happens especially for the first identified mode, whose difference with respect to the predicted value is significant for all the tests, apparently in a non-systematic way. This is perhaps due to the very low damping of the system, which makes the damping identification difficult especially for the lower frequencies. Starting from the experimental results, a deeper analysis is conducted to update the parameters used in the presented method. The updating process is carried out taking into account both natural frequencies and damping ratios, and the chosen parameters to be updated are:

- Length of the wire, L: the chosen initial value for the length of the wire is the distance between the supports. However, the effective length of the flexural vibrations may be different due to the definition of the boundary conditions.
- Young's modulus, E: the chosen initial value is the nominal value according to [18].
- Linear density, m: the chosen initial value is the nominal value according to [18].
- Measured axial force, T: its limits are reported in Table 3.
- Proportional damping coefficients α and β: the chosen initial values are obtained from the experimental system identification.

A multi-objective cost function that minimize the weighted RMSE (Root Mean Square Error) between analytic and experimental poles for each test is assembled, weighting the modes decreasingly from lower to higher according to eq. 33, where μ_i are the weights. A genetic algorithm [19] is used to find the best set of parameters.

$$\begin{cases} \min \sqrt{\sum_{i=1}^{n} \mu_i \left(\Re[s_{exp,i}] - \Re[s_{mod,i}]\right)^2}, & \sum_{i=1}^{n} \mu_i = 1 \\ \min \sqrt{\sum_{i=1}^{n} \mu_i \left(\Im[s_{exp,i}] - \Im[s_{mod,i}]\right)^2}, & \sum_{i=1}^{n} \mu_i = 1 \end{cases} \tag{33}$$

The results of the updating process are listed in Table 5, while Fig. 6 and Fig. 7 show the experimental frequencies and the identified poles respectively, compared with the outcomes of the presented method for the three tests. It can be seen that the updating process improves the correspondence between analytic and experimental results. In particular, the average error on the poles of the three tests decreases from 2.9% to 1.6%. It is important to highlight that the model relies on some assumptions that may be not respected in real measurements, in particular:

- The wire is considered simply supported, whilst the real boundary conditions are certainly different;
- The model is linear, while there may be some source of nonlinearities in the experimental setup.

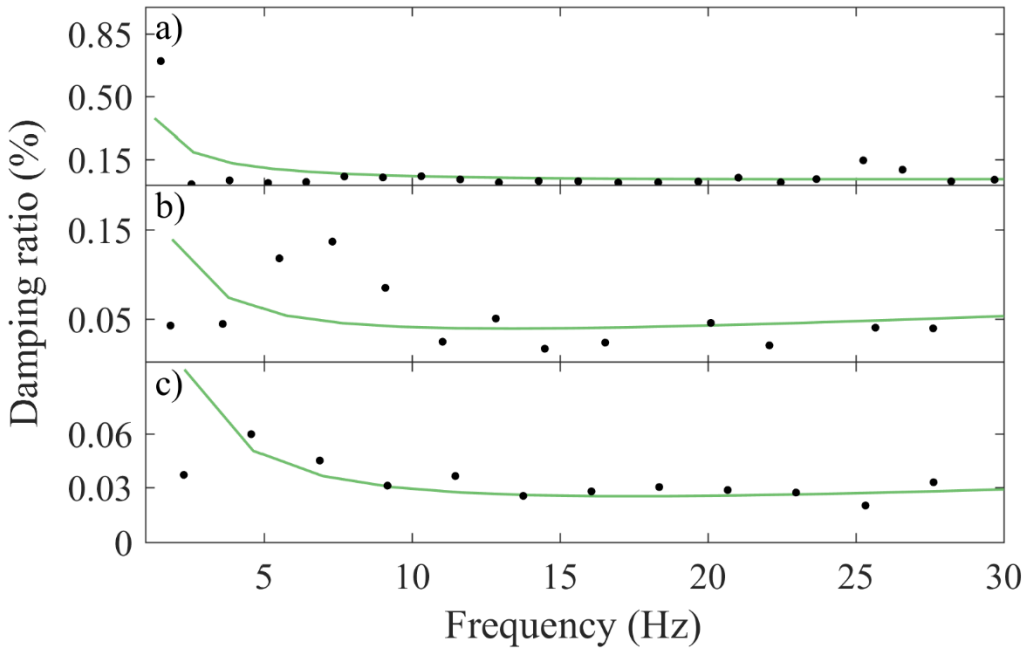

Fig. 5: Proportional damping model best fit. Black dot: experimental damping ratio. Green line: fitted results (least-square). a) Test 1, α=0.0562, β=2 10^{-6}. b) Test 2, α=0.0391, β=4 10^{-6}. c) Test 3, α=0.0315, β=2 10^{-6}.

		Original parameter	Updated parameter
Common parameters	Length of the contact wire (m)	30.70	30.57
	Young's Modulus (GPa)	120	121
	Linear density (kg/m)	0.889	0.866
Test 1	Tension (kN)	$5.17 \pm 6 \cdot 10^{-3}$	5.17
	α	0.0562	0.0536
	β	$2 \cdot 10^{-6}$	$3 \cdot 10^{-6}$
Test 2	Tension (kN)	$10.95 \pm 3\ 10^{-2}$	10.97
	α	0.0391	0.0378
	β	$4 \cdot 10^{-6}$	$5 \cdot 10^{-6}$
Test 3	Tension (kN)	$16.24 \pm 7 \cdot 10^{-2}$	16.26
	α	0.0315	0.0272
	β	$2 \cdot 10^{-6}$	$2 \cdot 10^{-6}$

Table 5: Model updated parameters for Test 1, 2, 3.

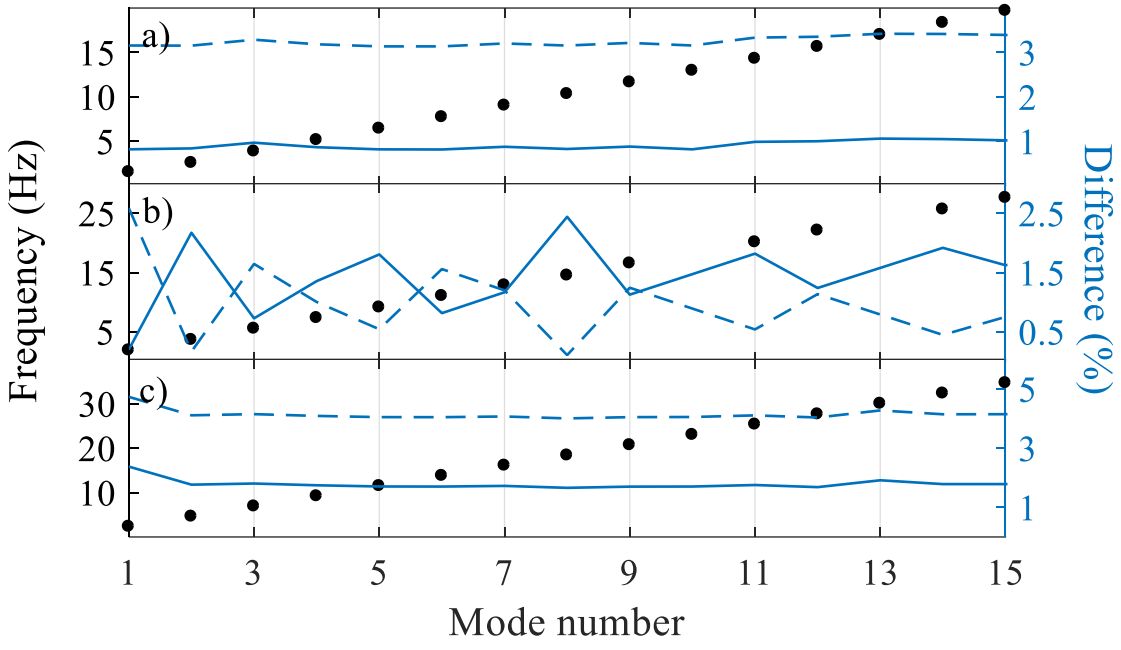

Fig. 6: Natural frequencies of the system. Black dot: experimental frequency. Dashed blue line: percentage difference between analytic and experimental frequencies before the update. Blue line: percentage difference between analytic and experimental frequencies after the update. a) Test 1. b) Test 2. c) Test 3.

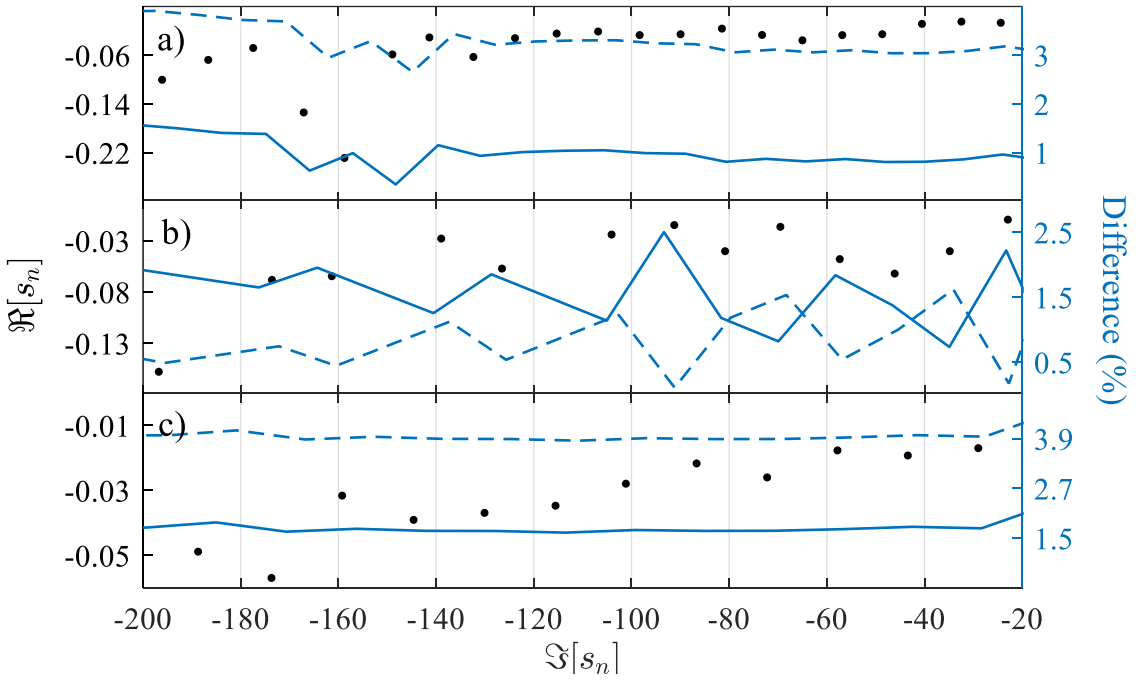

Fig. 7: Poles of the system. Black dot: identified experimental pole. Dashed blue line: percentage difference between analytic and experimental poles before the update. Blue line: percentage difference between analytic and experimental poles after the update. a) Test 1. b) Test 2. c) Test 3.

The final results show that a good representation of the real damping distribution is obtained by using a coefficient α in the range 0.06-0.02 when the axial force is between 5-16 kN respectively, while the coefficient β is in the order of 10^{-6}. It is worth noticing that these values are in the same range of those presented in the other previously mentioned studies [6-10], even though they are related to different catenary systems and obtained with different methods. In particular, a key issue related to the damping distribution is the propagation of waves across the overhead contact line, which is certainly different for different systems. The moving load exerted by the pantograph causes dispersive waves to travel along the catenary system, with lots of reflections due to droppers, clamps, suspensions. This generally may result in an amplification of the vibrations, as well as the stress acting on the wires [20]. Nevertheless, it is difficult to clearly describe the wave reflection phenomenon in such complex systems, especially when dealing with experimental measurements. Therefore, it is not straightforward to link the effects of wave reflections on the damping distribution in the considered system with the phenomena occurring in complete overhead contact lines. A representation of wave propagation in the considered setup is reported in the following section (Fig. 10).

The proposed practical application is well described by a proportional damping distribution in the frequency range of interest, but the presented method, as well as the optimization procedure adopted, is still valid even in the case of a non-proportional distribution. The latter case, involving again the considered contact wire, is discussed in the following section.

3.2. **Contact wire with a lumped damper**

A second series of experiments is performed on the same system of Fig. 1 with the addition of a lumped commercial damper, to test the capability of the model to handle a non-proportional damping distribution. The damper used in these tests has been chosen for its easy availability and high damping properties, which ensure a significant non-proportionality of the damping distribution. Realistically, the use of specifically designed damping elements in overhead contact lines has been studied in the recent years to improve the current collection quality. For instance, in [21] damper hangers are added to a PHC catenary equipment to increase the train velocity on the Hokuriku Shinkansen line.

A representation of the test rig is reported in Fig. 8a, while a picture of the damper is shown in Fig. 8b. The position of the damper is $L_w = 9$ m from the left-hand side.

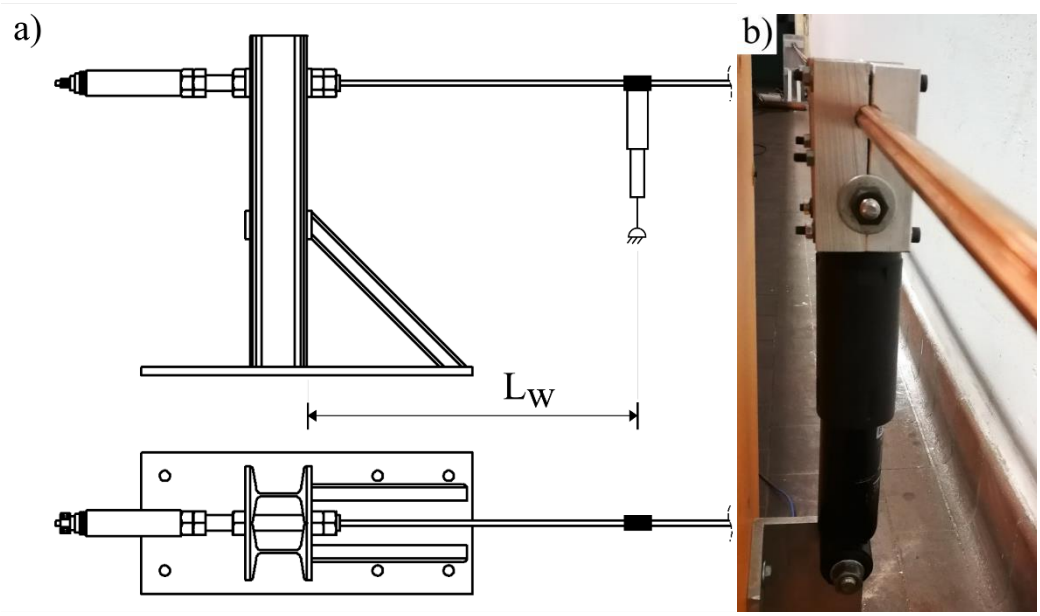

Fig. 8: a) Scheme of the second test bench. b) Photo of the damper, at L_w=9 m.

All the tests are performed applying an impulse load along the z-axis and recording the accelerations of five different points, as reported in Table 6. One level of tension is considered according to Table 7.

Accelerometer n°	1	2	3	4	5
Position (m)	1.5	9	13	17	22

Table 6: Position of the accelerometers measured from the left end (case with lumped elements).

Test	Tensile load T (kN)	Sampling frequency f_s (Hz)	Acquisition time t (s)
4	$14.83 \pm 1 \cdot 10^{-2}$	81.92	300

Table 7: Test performed on the contact wire with a lumped damper. The tensile load is written as mean value ± variation.

The configuration shown in Fig. 8 can be seen as a two-segments system having the same transversal section; thus, the equation of motion can be written as follows:

$$m\frac{\partial^2 w}{\partial t^2} + c_{ex,p}\frac{\partial w}{\partial t} + c_{in,p}^{k}\frac{\partial^4}{\partial x^4}\left(\frac{\partial w}{\partial t}\right) - c_{in,p}^{T}\frac{\partial^2}{\partial x^2}\left(\frac{\partial w}{\partial t}\right) + k\frac{\partial^4 w}{\partial x^4} - T\frac{\partial^2 w}{\partial x^2} = f(x,t) \quad p = 1,2 \tag{34}$$

The connection between the two segments is given by the physical damper and is represented by a lumped mass M_w, a lumped stiffness K_w and a lumped damping C_w, as shown in Fig. 9.

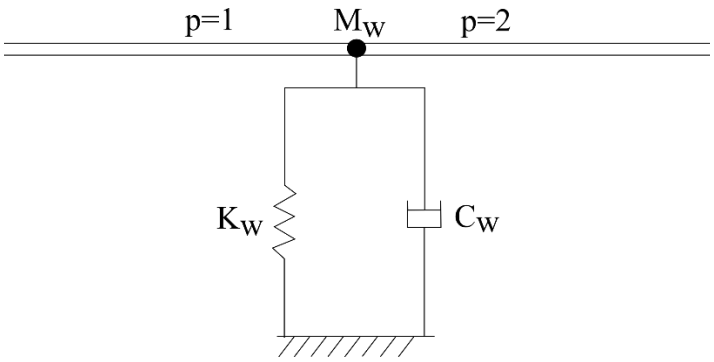

Fig. 9: Modelling of the lumped damper.

The introduction of a damping device deeply changes the dynamics of the considered system. A preliminary test with a high sampling frequency (102.4 kHz) is conducted to highlight the transversal wave propagation due to an impulse load applied at 29 m from the left-hand side. A comparison in terms of displacements is reported in Fig. 10: waves propagate from one end to the other when the damper is not present, while a discontinuity is clearly visible when the damper is mounted. This results in a very low excitation on the first accelerometer, positioned at 1.5 m, as the two parts of the contact wire are almost uncoupled.

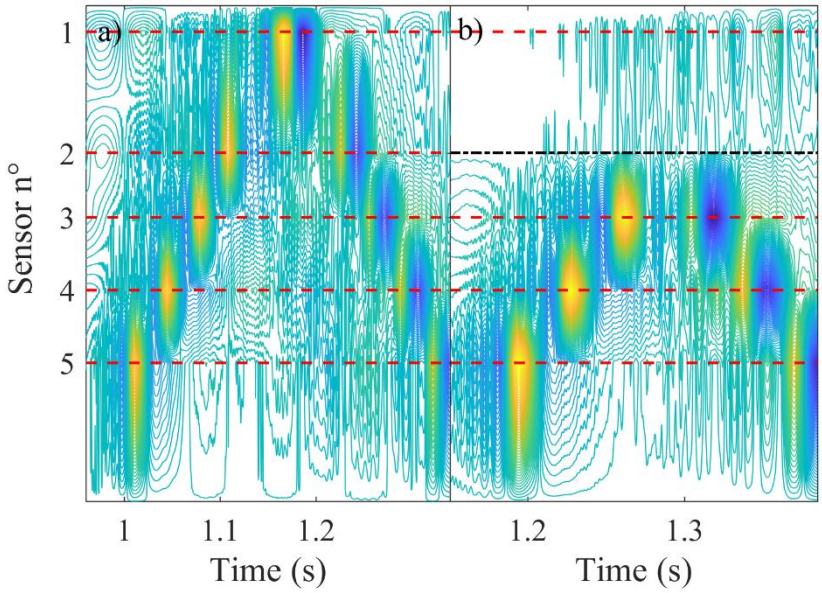

Fig. 10: Contour plot of the displacements measured along the contact wire. Red dashed line: position of an accelerometer. Black dashed-dotted line: position of the damper. a) Case without the damper. b) Case with the damper.

3.2.1. System identification

A linear subspace identification technique [13] is used also in this case to extract the modal parameters from the described system. The system identification procedure is the same of paragraph 3.1.1, as well as the criteria adopted to select the order of each mode. However, the MACX [22] is used instead of the MAC, to account for the non-proportional damping distribution. The stabilization diagram is depicted in Fig. 11, while the identified parameters according to the criteria C1 and C2 (see paragraph 3.1.1) are listed in Table 8. The modes related to the y-axis are discarded and the MACXs between C1 and C2 are computed to verify that each identified mode is the same for the different criteria. The best order for each mode is then chosen according to C1.

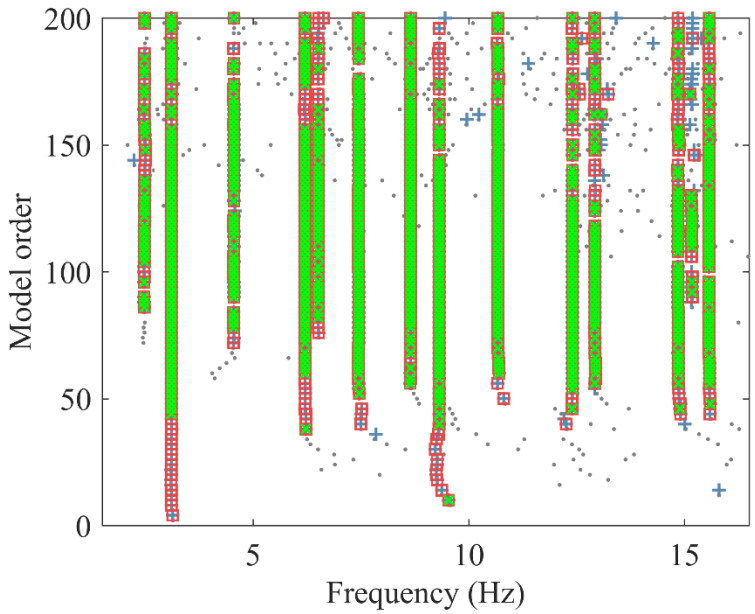

Fig. 11: Stabilization diagram for Test 4. Stabilization thresholds for natural frequency, damping ratio and MAC are 0.5%, 10% and 99.5%, respectively. Grey dot: new (not stable) pole. Blue plus: pole stable in frequency. Red square: pole stable in frequency and MACX. Green cross: pole stable in frequency, MACX and damping.

Frequency, f_{exp} (Hz)		Damping ratio, ζ_{exp} (%)	
C1	C2	C1	C2
2.478	*2.475*	*1.410*	*1.442*
3.108	3.108	0.276	0.269
4.551	*4.551*	*1.393*	*1.405*
6.363	6.363	0.150	0.148
6.511	*6.511*	*0.197*	*0.199*
7.443	7.443	0.454	0.468
8.647	*8.647*	*0.265*	*0.262*
9.312	9.312	0.208	0.201
10.673	*10.673*	*0.320*	*0.323*
12.404	12.403	0.077	0.071
12.921	*12.921*	*0.104*	*0.104*
14.852	14.852	0.287	0.289
15.571	15.569	0.163	0.148

Table 8: Identified modes for Test 4. Italics red color highlights modes related to the y-axis. C1 and C2 are the two different criteria.

3.2.2. **Study on the root locus**

An effective way to study the sensitivity of the model to each lumped parameter is to track the root locus as the selected parameter evolves, as shown in [11]. Fig. 12 shows the locus of the first 4 poles when the value of the lumped damping C_w increases from 0 Ns/m to 10^5 Ns/m: a fixed value for K_w is adopted and no lumped mass is considered. Each pole evolves in the complex plane and asymptotically tends to the "uncoupled" configuration (for high values of C_w), defined as the configuration in which the damper acts like a fixed point. The black dashed lines represent the imaginary part of the poles in this configuration. It is also worth noticing a "jump" between the second and the third mode, so that their final configuration is reversed with respect to the starting position.

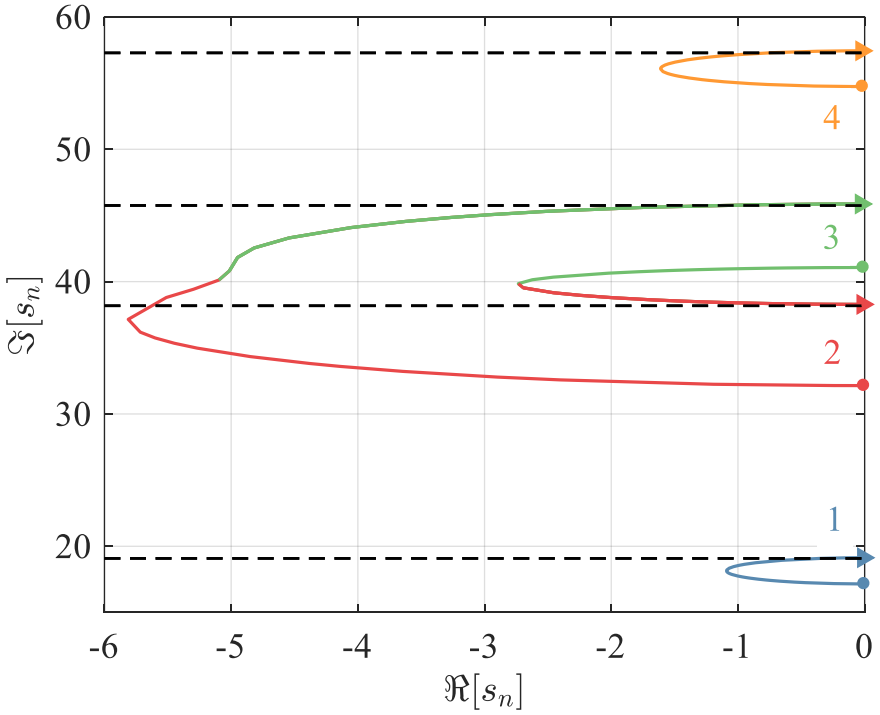

Fig. 12: Locus of the first four poles for increasing values of the lumped damping. Black dashed lines: imaginary part of the poles in the "uncoupled" configuration.

A more comprehensive picture can be obtained considering also several levels for the stiffness K_w, as in Fig. 13, showing the locus of the second pole split in its real and imaginary parts. The different lines correspond to different values of K_w and are plotted with different colors. The considered values are 5 N/mm, 10 N/mm, 50 N/mm, and 100 N/mm.

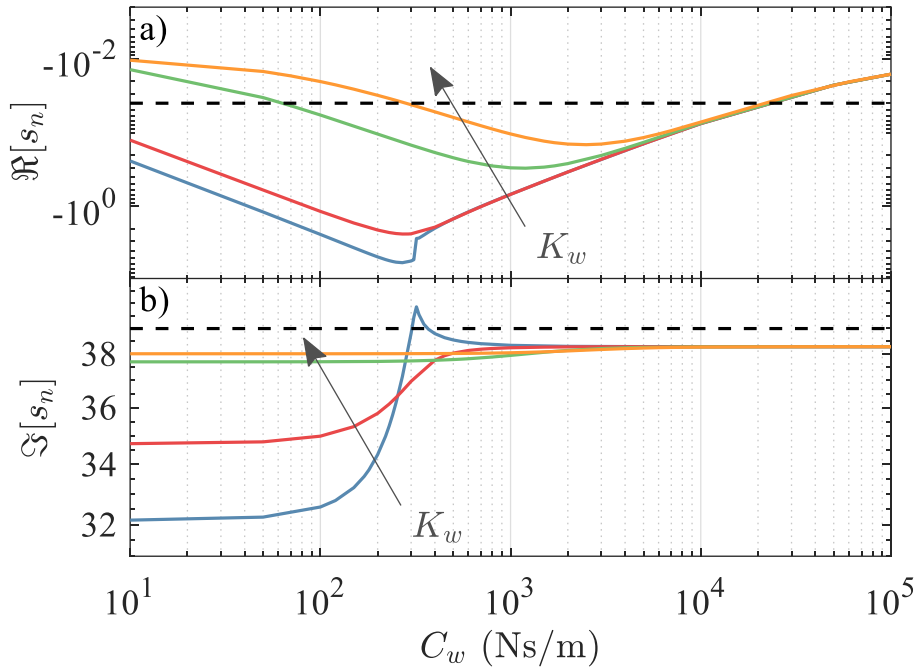

Fig. 13: Root locus of the second pole for increasing values of the lumped damping C_w and for several values of the lumped stiffness K_w: 5 N/mm (blue), 10 N/mm (red), 50 N/mm (green), 100 N/mm (orange). a) Real part of the pole. b) Imaginary part of the pole. Dashed black lines: identified real and imaginary parts.

Jumps are observed for low values of K_w as in Fig. 12, while the transition is smoother for higher values. Moreover, the root locus seems to be independent from the value of K_w for high values of C_w, i.e. as $C_w \to +\infty$. It is obvious that the value of C_w would also become negligible as $K_w \to +\infty$, because the uncoupled configuration would be reached. Recalling that the aim of this test is to find the values of the lumped coefficients that minimize the distance between experimental and analytic poles, it is clear from Fig. 13 that the solution may generally not be unique, and it should be sought in a feasible range for K_w and C_w. Furthermore, the model updating is conducted on all the identified poles together, thus Fig. 14 shows the tracking of the seven considered poles, selecting again several values of K_w and increasing C_w from 0 Ns/m to 10^5 Ns/m. Each value of the lumped stiffness corresponds to a specific color, while the black crosses represent the experimentally identified poles.

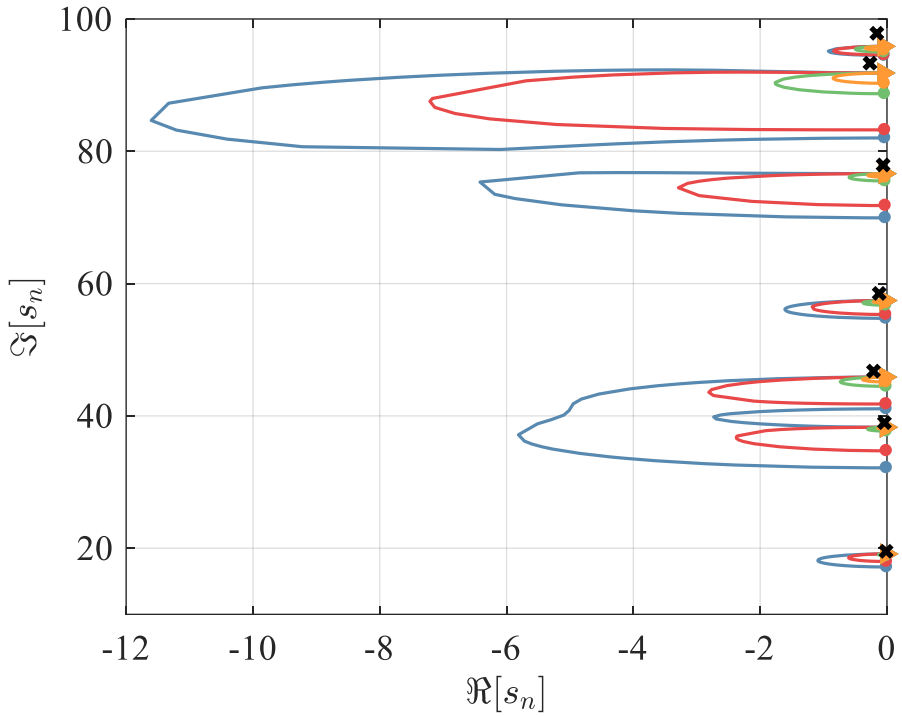

Fig. 14: Root locus of the first seven poles for increasing values of the lumped damping C_w and for several values of the lumped stiffness K_w: 5 N/mm (blue), 10 N/mm (red), 50 N/mm (green), 100 N/mm (orange). Black crosses: identified poles.

A model updating procedure is finally implemented in the following section to find the best-fit between experimental poles and analytic ones.

3.2.3. **Damping distribution and model updating**

Starting from the experimental results, a deeper analysis is conducted to update the parameters used in the presented method. The model updating uses the same tools as in paragraph 3.1.2, and the parameters to be updated are: the tensile force T, the position of the damper L_w, the lumped damping C_w, the lumped stiffness K_w, the lumped mass M_w, the damping coefficients $c_{ex,p}, c_{in,p}^k, c_{in,p}^T$ with $p = 1, 2$. The starting values for the damping coefficients are obtained performing a prior experimental measurement removing the damper and maintaining the same level of tensile force, and are listed in Table 9. In this case a proportional distribution is obtained, thus the damping coefficients are related to α and β according to eq. 31. The feasible range for the lumped stiffness and damping is chosen considering the experimental identification conducted in [23] on a similar device, and taking the linearized values there obtained as starting points. The other common parameters are selected from the already

updated values listed in Table 5. The results of the model updating are listed in Table 9, while a comparison between experimental and analytic poles is reported both in Table 10 and Fig. 15.

	Original parameter	Updated parameter
Position of the damper (m)	9	8.9
Tension (kN)	14.83 ± 0.11	14.93
Lumped damping C_w (Ns/m)	$2 \cdot 10^3$ (1)	$7 \cdot 10^3$
Lumped mass M_w (kg)	-	0.4
Lumped stiffness K_w (N/m)	$50 \cdot 10^3$ (1)	$87 \cdot 10^3$
Damping coefficient $c_{ex,1}$ (Ns/m^2)	$7 \cdot 10^{-2}$ (2)	$5 \cdot 10^{-2}$
Damping coefficient $c_{in,1}^k$ (Nsm^2)	$5 \cdot 10^{-4}$ (2)	$3 \cdot 10^{-5}$
Damping coefficient $c_{in,1}^T$ (Ns)	$9 \cdot 10^{-2}$ (2)	$8 \cdot 10^{-6}$
Damping coefficient $c_{ex,2}$ (Ns/m^2)	$7 \cdot 10^{-2}$ (2)	$4 \cdot 10^{-2}$
Damping coefficient $c_{in,2}^k$ (Nsm^2)	$5 \cdot 10^{-4}$ (2)	$8 \cdot 10^{-6}$
Damping coefficient $c_{in,2}^T$ (Ns)	$9 \cdot 10^{-2}$ (2)	$6 \cdot 10^{-6}$

Table 9: Model updated parameters for Test 4. The values marked with (1) are obtained from [23]. The values marked with (2) are obtained from a prior experimental identification without the damper.

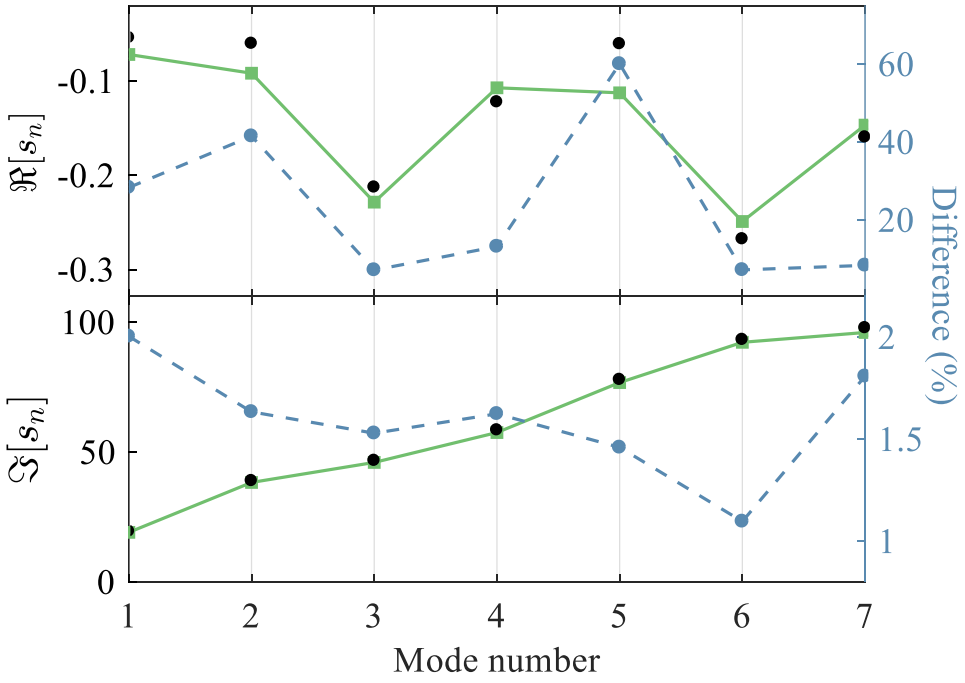

Fig. 15: Poles of the system for Test 4. Black dot: identified experimental pole. Continue green line: analytic poles. Dashed blue line: percentage difference between analytic and experimental poles.

Mode number	Experimental pole	Analytic pole (after the optimization)
1	$-0.054 + 19.529i$	$-0.072 + 19.142i$
2	$-0.060 + 39.985i$	$-0.092 + 38.352i$
3	$-0.212 + 46.769i$	$-0.228 + 46.059i$
4	$-0.122 + 58.510i$	$-0.107 + 57.568i$
5	$-0.060 + 77.934i$	$-0.112 + 76.804i$
6	$-0.268 + 93.320i$	$-0.249 + 92.301i$
7	$-0.159 + 97.836i$	$-0.147 + 96.083i$

Table 10: Experimental and analytic poles for Test 4.

A good agreement is achieved between analytic and experimental poles also in this case. In particular, all the first seven modes are well identified and modelled, though some distinct differences are present between some of the poles. These errors between measurements and predictions are very likely to be associated with two key factors:

- Uncertainties in the identification process, as the correct identification of the damping is generally critical;
- The adoption of a linear model for the damper, which may not be the best one.

A detailed characterization of the damper is not the object of this study, because it would certainly require nonlinear tools ([15, 23]). Instead, the focus of this test is on the capability of the proposed method to handle highly non-proportional damping distributions.

4. CONCLUSIONS

The paper proposes a method to characterize the dynamic properties of a railway contact wire, and experimental tests have been performed both to validate the model and to estimate the damping distribution of the system. Two experimental setups are presented with a proportional and a non-proportional damping distribution respectively. The final results show that a good representation of the real damping distribution is obtained in both cases, and some useful indications on the damping properties of the contact wire are provided as well. The proportional damping model better fits the experimental measurements when no external damping elements are present, with coefficient α in the range 0.06-0.02 when the axial force is between 5-16 kN respectively, and coefficient β in the order of 10^{-6}. Further investigations should be conducted considering more levels of tension, in order to estimate a relation between the axial force and the proportional damping parameters. If external lumped dampers are added, the damping distribution dramatically changes and the proportional model cannot be adopted. The resulting damping distribution is of course related to the characteristics of the lumped damper. It is worth highlighting that the results presented in this study may not be extended to the entire catenary system, in which several other components are present. The purpose of this study is to characterize the contact wire, considered the most important part of the overhead contact line. More realistic tests involving droppers and clamps should be performed, in order to verify how the damping distribution of the overhead contact line is influenced by those elements.

REFERENCES

[1] G. Poetsch, J. Evans, R. Meisinger, W. Kortum, W. Baldauf, A. Veitl, J. Wallaschek, Pantograph/Catenary Dynamics and Control, Vehicle System Dynamics: International Journal of Vehicle Mechanics and Mobility, 28(2-3), 1997, 159-195.

[2] S.Y. Park, B.U. Jeon, M.J. Lee, Y.H. Cho, Measurement of low–frequency wave propagation in a railway contact wire with dispersive characteristics using wavelet transform, Key Engineering Materials, 321–323, 2006, 1609–1615.

[3] T. Dahlberg, Moving force on an axially loaded beam—with applications to a railway overhead contact wire, Vehicle System Dynamics: International Journal of Vehicle Mechanics and Mobility, 44(8), 2006, 631-644.

[4] BS EN 50318:2002, Railway applications. Current collection systems. Validation of simulation of the dynamic interaction between pantograph and overhead contact line. BSI, 2002.

[5] J.P. Massat, T.M.L. Nguyen-Tajan, H. Maitournam, E. Balmes, Fatigue analysis of catenary contact wires for high speed trains, 9th World Congress on Railway Research, Lille, France, May 2011, 1-11.

[6] J. Ambrosio, J. Pombo, M. Pereira, P. Antunes and A. Mósca, A Computational Procedure for the Dynamic Analysis of the Catenary-Pantograph Interaction in High-Speed Trains, Journal of Theoretical and Applied Mechanics/Poland, 50 (3), 2012, 681-699.

[7] J. Ambrosio, J. Pombo, P. Antunes, M. Pereira, PantoCat statement of method, Vehicle System Dynamics, 53 (3), 2015, 314-328.

[8] S. Bruni et al., The results of the pantograph–catenary interaction benchmark, Vehicle System Dynamics, 53 (3), 2015, 412-435.

[9] P. Nåvik, A. Rønnquist, S. Stichel, Identification of system damping in railway catenary wire systems from full-scale measurements, Engineering Structures, 113, 2016, 71-78.

[10] Y.H. Cho, J.M. Lee, S.Y. Park, E.S. Lee, Robust Measurement of Damping Ratios of a Railway Contact Wire Using Wavelet Transforms, Key Engineering Materials, 321-323, 2006, 1629-1635.

[11] S. Sorrentino, S. Marchesiello, B. Piombo, A new analytical technique for vibration analysis of non–proportionally damped beams, Journal of Sound and Vibration, 265, 2003, 765–782.

[12] S. Sorrentino, A. Fasana, S. Marchesiello, Frequency domain analysis of continuous systems with viscous generalized damping, Shock and Vibration, 11, 2004, 243-259.

[13] P. Van Overschee, B. De Moor, Subspace identification for linear systems, Kluwer Academic Publishers, 1996.

[14] E. Gandino, L. Garibaldi, S. Marchesiello, Covariance-driven subspace identification: A complete input–output approach, Journal of Sound and Vibration, 332, 2013, 7000-7017.

[15] S. Marchesiello, A. Fasana, L. Garibaldi, Modal contributions and effects of spurious poles in nonlinear subspace identification, Mechanical Systems and Signal Processing, 74, 2016, 111-132.

[16] L. Meirovitch, Principles and techniques of vibrations, Prentice Hall, 1999.

[17] J.F. Bonnans, J.C. Gilbert, C. Lemarechal, C.A. Sagastizábal, Numerical Optimization, Springer, 2006.

[18] BS EN 50149:2001, Railway applications. Fixed installations. Electric traction. Copper and copper alloy grooved contact wires., BSI, 2001.

[19] K. Deb, Multi-Objective Optimization Using Evolutionary Algorithms, John Wiley & Sons, 2001.

[20] S. Sorrentino, D. Anastasio, A. Fasana, S. Marchesiello, Distributed parameter and finite element models for wave propagation in railway contact lines, Journal of Sound and Vibration, 410, 2017, 1-18.

[21] S. Harada, M. Shimizu, K. Ikeda, J. Sato, S. Koyano, K. Chikanari, Development of Simple Catenary Equipment Using PHC Contact Wire for Sinkansen, QR of RTRI, 49 (2), 2008, 96-102.

[22] P. Vacher, B. Jacquier, A. Bucharles, Extensions of the mac criterion to complex modes, Proceedings of ISMA2010 including USD2010, Leuven, November 2010, 2713–2726.

[23] A. Audenino, G. Belingardi, L. Garibaldi, Uso del “Restoring Force Mapping” per lo studio del comportamento dinamico di ammortizzatori autoveicolistici, Atti X Congresso Nazionale dell’Associazione Italiana di Meccanica Teorica ed Applicata, Pisa, October 1990.

FIGURE CAPTIONS

Fig. 1: The experimental setup.

Fig. 2: a) Scheme of the tensioning device and section of the contact wire. b) Photo of the test bench.

Fig. 3: Power spectral density of the acceleration recorded by the second accelerometer during the test 3. Solid blue line: z-axis. Dashed red line: y-axis.

Fig. 4: Stabilization diagram for Test 1. Stabilization thresholds for natural frequency, damping ratio and MAC are 0.5%, 10% and 99.5%, respectively. Grey dot: new (not stable) pole. Blue plus: pole stable in frequency. Red square: pole stable in frequency and MAC (Modal Assurance Criterion). Green cross: pole stable in frequency, MAC and damping.

Fig. 5: Proportional damping model best fit. Black dot: experimental damping ratio. Green line: fitted results (least-square). a) Test 1, α=0.0562, β=2 10^{-6}. b) Test 2, α=0.0391, β=4 10^{-6}. c) Test 3, α=0.0315, β=2 10^{-6}.

Fig. 6: Natural frequencies of the system. Black dot: experimental frequency. Dashed blue line: percentage difference between analytic and experimental frequencies before the update. Blue line: percentage difference between analytic and experimental frequencies after the update. a) Test 1. b) Test 2. c) Test 3.

Fig. 7: Poles of the system. Black dot: identified experimental pole. Dashed blue line: percentage difference between analytic and experimental poles before the update. Blue line: percentage difference between analytic and experimental poles after the update. a) Test 1. b) Test 2. c) Test 3.

Fig. 8: a) Scheme of the second test bench. b) Photo of the damper, at L_w=9 m.

Fig. 9: Modelling of the lumped damper.

Fig. 10: Contour plot of the displacements measured along the contact wire. Red dashed line: position of an accelerometer. Black dashed-dotted line: position of the damper. a) Case without the damper. b) Case with the damper.

Fig. 11: Stabilization diagram for Test 4. Stabilization thresholds for natural frequency, damping ratio and MAC are 0.5%, 10% and 99.5%, respectively. Grey dot: new (not stable) pole. Blue plus: pole stable in frequency. Red square: pole stable in frequency and MACX. Green cross: pole stable in frequency, MACX and damping.

Fig. 12: Locus of the first four poles for increasing values of the lumped damping. Black dashed lines: imaginary part of the poles in the “uncoupled” configuration.

Fig. 13: Root locus of the second pole for increasing values of the lumped damping Cw and for several values of the lumped stiffness Kw: 5 N/mm (blue), 10 N/mm (red), 50 N/mm (green), 100 N/mm (orange). a) Real part of the pole. b) Imaginary part of the pole. Dashed black lines: identified real and imaginary parts.

Fig. 14: Root locus of the first seven poles for increasing values of the lumped damping Cw and for several values of the lumped stiffness Kw: 5 N/mm (blue), 10 N/mm (red), 50 N/mm (green), 100 N/mm (orange). Black crosses: identified poles.

Fig. 15: Poles of the system for Test 4. Black dot: identified experimental pole. Continue green line: analytic poles. Dashed blue line: percentage difference between analytic and experimental poles.

TABLES